ADVANCED ENERGY MATERIALS
www.advenergymat.de

Atmospheric-Pressure Chemical Vapor Deposition of Iron Pyrite Thin Films

*Nicholas Berry, Ming Cheng, Craig L. Perkins, Moritz Limpinsel, John C. Hemminger, and Matt Law**

Iron pyrite (cubic FeS_2) is a promising candidate absorber material for earth-abundant thin-film solar cells. In this report, single-phase, large-grain, and uniform polycrystalline pyrite thin films are fabricated on glass and molybdenum-coated glass substrates by atmospheric-pressure chemical vapor deposition (AP-CVD) using the reaction of iron(III) acetylacetonate and *tert*-butyl disulfide in argon at 300 °C, followed by sulfur annealing at 500–550 °C to convert marcasite impurities to pyrite. The pyrite-marcasite phase composition depends strongly on the concentration of sodium in the growth substrate and the sulfur partial pressure during annealing. Phase and elemental composition of the films are characterized by X-ray diffraction, Raman spectroscopy, Auger electron spectroscopy, secondary ion mass spectrometry, Rutherford backscattering spectrometry, and X-ray photoelectron spectroscopy. The in-plane electrical properties are surprisingly insensitive to phase and elemental impurities, with all films showing *p*-type, thermally activated transport with a small activation energy (≈30 meV), a room-temperature resistivity of ≈1 Ω cm, and low mobility. These ubiquitous electrical properties may result from robust surface effects. These CVD pyrite thin films are well suited to fundamental electrical studies and the fabrication of pyrite photovoltaic device stacks.

1. Introduction

Iron pyrite (FeS_2) is a promising photovoltaic (PV) material because of its suitable bandgap (E_g = 0.95 eV), strong light absorption ($\alpha > 10^5$ cm^{-1} for $h\nu > 1.4$ eV), long minority carrier diffusion lengths (100–1000 nm), and essentially infinite elemental abundance, which makes it particularly exciting for multiterawatt PV deployment.[1–4] Unfortunately, pyrite devices suffer from a low open-circuit photovoltage (V_{OC}): under standard test conditions, the best pyrite photoelectrochemical and solid-state Schottky solar cells show large photocurrents (30–42 mA cm^{-2}) but V_{OC} < 200 mV (about 20% of the bandgap) and efficiencies of ≈3%.[5–10] Since 1984, a number of studies have explored possible causes of the low V_{OC}, including bulk or near-surface nonstoichiometry (usually ascribed to sulfur vacancies),[11–13] midgap defect states that cause surface Fermi level pinning, thermionic-field emission, and large dark currents,[11,14–16] metallic FeS-like surface layers,[17,18] and domains of small-gap phases in the pyrite bulk (including pyrrhotite, marcasite, and amorphous iron sulfide phases).[11,19] To date, there is no consensus as to the cause of the low V_{OC} or the nature of the alleged gap states. Enhancing the photovoltage and efficiency of pyrite solar cells requires basic research on the growth, structural and electronic characterization, and bulk and surface defect passivation of pyrite thin films.

Pyrite can be described as $Fe^{2+}S_2^{2-}$, in which the sulfur ions are paired into persulfide dimers. The crystal structure is similar to rock salt (space group $pa\bar{3}$), with a face-centered cubic (FCC) sublattice of Fe^{2+} ions and sulfur dumbbells pointed along the <111> directions occupying the anion sites.[20] This arrangement results in a slightly distorted octahedral coordination for Fe^{2+}, which exists in its diamagnetic d^6 configuration, and tetrahedral coordination of each sulfur atom to three iron ions and its dimer partner. The basic electronic structure of pyrite has been the subject of extensive experimental[21–25] and theoretical studies.[18,26–30] The top of the valence band is formed by the overlap of mostly nonbonding Fe 3d t_{2g} states, while the bottom of the conduction band is composed primarily of Fe e_g^* and S ppσ^* states.

Pyrite thin films have been prepared by many techniques, including the sulfurization of iron thin films,[31–37] sputtering,[38–41] flash evaporation,[42,43] electrodeposition,[44,45] spray pyrolysis,[46] molecular beam epitaxy,[47] and chemical vapor deposition (CVD). Pyrite growth by CVD has been studied mainly by three research groups using three different CVD chemistries (see **Table 1**). The Tributsch group at the Hahn-Meitner Institut

N. Berry
Department of Physics
University of California
Irvine, CA 92697, USA
M. Cheng, M. Limpinsel, Prof. J. C. Hemminger, Prof. M. Law
Department of Chemistry
University of California
Irvine, CA 92697, USA
E-mail: matt.law@uci.edu
Dr. C. L. Perkins
National Renewable Energy Laboratory
Golden, CO 8040, USA

DOI: 10.1002/aenm.201200043

© 2012 WILEY-VCH Verlag GmbH & Co. KGaA, Weinheim

Table 1. Pyrite thin films made by CVD. IPC, iron pentacarbonyl; TBDS, tert-butyl disulfide; TAA, thioacetamide.

Chemistry	Substrate	T [°C]	P [Torr]	Composition and properties	Ref
IPC, H_2S/S	Glass	130–140	760	$FeS_{1.9}$,[a] p-type,[d] $\rho = 2\ \Omega$ cm	[48]
IPC, TBDS	Steel, Al	480	5	–	[49]
IPC, TBDS	Glassy C	500–600	38	$FeS_{2.0-2.04}$,[b] p-type[d]	[64]
IPC, S	Glassy C	300 + A[f]	760	$FeS_{2.0-2.04}$,[b] p-type[d]	[64]
IPC, TBDS	Various	525–630	38	$FeS_{1.99-2.03}$[b]	[52]
IPC, TBDS	Si, GaP, ZnS	450–500	38	$FeS_{1.99\text{-}2.01}$,[b] no epitaxy	[53]
IPC, TBDS	Pyrite, ZnS	475	38	Epitaxy on pyrite, not ZnS; $\rho = 2\ \Omega$ cm	[54]
IPC, TBDS	Glass, carbon	475	38	$FeS_{1.98\text{-}2.02}$,[b] p-type,[d] $\rho = 1\ \Omega$ cm	[55]
IPC, TBDS	Glass	425	38	$Fe_{0.92}Co_{0.078}S_2$,[b] n-type[d),e)] $\rho = 0.005\ \Omega$ cm, $\mu_H = 2.4$ cm^2 V^{-1} s^{-1}	[56]
$FeCl_3$, TAA	Glass	450–550	760	$FeS_{1.94}$,[c] n-type,[e] $\rho = 10\ \Omega$ cm $\mu_H = 20$ cm^2 V^{-1} s^{-1}	[57]
$FeCl_3$, TAA	Silicon	400	760	epilayer, $FeS_{1.98}$,[c] n-type[e] $\rho = 10\ \Omega$ cm, $\mu_H = 280$ cm^2 V^{-1} s^{-1}	[58]
$Fe(acac)_3$, TBDS, H_2	Glass	300–340	8	$FeS_{1.98-2.08}$,[b] p-type,[d] $\rho = 1\ \Omega$ cm	[59]
$Fe(acac)_3$, TBDS	Glass, Si, moly/glass	300 + A[f]	760	$FeS_{2.00\pm0.06}$, p-type,[d] $\rho = 1\ \Omega$ cm	This work

[a] α = by microprobe; [b] by RBS; [c] by energy dispersive sepctroscopy (EDS); [d] by thermopower; [e] by Hall effect; [f] annealed in sulfur vapor.

in Berlin used iron pentacarbonyl (IPC) as an iron source and H_2S, sulfur, *tert*-butyl sulfide (TBS), or *tert*-butyl disulfide (TBDS) as the sulfur source at temperatures of 130–600 °C at both atmospheric and low pressure.[48–55] Nominally undoped films made with IPC were reported to be p-type with low values of dark resistivity (0.1–1.0 Ω cm), thermopower (<70 μV K^{-1}), and carrier mobility (<0.1 cm^2 V^{-1} s^{-1}) at room temperature. Relatively high temperatures (>450 °C) and high sulfur precursor pressures were needed to avoid the formation of marcasite (orthorhombic FeS_2) and pyrrhotite (monoclinic or hexagonal $Fe_{1-x}S$) phase impurities, the latter of which appear to be particularly detrimental to the optoelectronic properties of pyrite films.[55] Films made at sufficiently high sulfur precursor pressures showed S:Fe ratios of 2.02 ± 0.02 by Rutherford backscattering spectrometry (RBS).[52] Excess sulfur has been alleged to cause p-type doping (via iron vacancies acting as acceptors),[51] but the evidence for iron vacancies or sulfur interstitials is weak and any excess sulfur may reside at grain boundaries rather than lattice sites. Intentional doping with cobalt was demonstrated to produce n-type films.[56]

The Nakamura group in Japan has explored the growth of polycrystalline pyrite films on glass substrates using $FeCl_3$ and thioacetamide at 450–550 °C at atmospheric pressure.[57] The films showed n-type conductivity (presumably from chlorine doping, since nominally undoped pyrite single crystals made by chemical vapor transport (CVT) with halogen transport agents are n-type[60–63] and density functional theory modeling shows that Cl acts as a donor in pyrite),[64] a relatively high resistivity of 1–10 Ω cm, and a Hall mobility of 20 cm^2 V^{-1} s^{-1}. These authors later extended their approach to grow micron-thick pyrite epilayers on silicon (100) substrates at 400 °C. These films showed an S:Fe ratio of 1.98, n-type conductivity, and Hall mobilities as high as 280 cm^2 V^{-1} s^{-1}.[58] This remarkable epilayer result has apparently not been pursued further or reproduced by other groups.

Goossens, Schoonman, and co-workers[59,65] synthesized 100 nm thick pyrite films using iron(III) acetylacetonate [$Fe(acac)_3$], TBDS, and H_2 mixtures at 300–340 °C. These authors reported that hydrogen was required for film growth. The films showed S:Fe ratios of 1.98–2.07 by RBS, appreciable oxygen, carbon, and hydrogen content by elastic recoil detection analysis (≈0.4 at%, ≈2 at%, and ≈1 at%, respectively), p-type conductivity (positive Seebeck coefficients of 30–70 μV K^{-1} at room temperature), and dark resistivities of 0.5–1.0 Ω cm. The films made with $Fe(acac)_3$ show strikingly similar electrical properties to films grown with IPC.

In this report, we present single-phase, large-grain, and uniform polycrystalline pyrite thin films grown on glass and molybdenum-coated glass substrates by CVD using the reaction of $Fe(acac)_3$ and TBDS at 300 °C and atmospheric pressure without hydrogen, followed by sulfur annealing at 500–550 °C to convert marcasite impurities to pyrite. $Fe(acac)_3$ was selected as the iron source to avoid IPC, which is a thermally unstable and highly toxic precursor, and $FeCl_3$ or other halide salts, which are expected to dope the films n-type with halogen donors. We show that hydrogen is not required to produce FeS_2 films. The annealed films are rigorously phase pure by XRD, Raman spectroscopy, and initial magnetic susceptibility measurements and possess appropriate morphological and optical characteristics for application in solar cells. Auger electron spectroscopy (AES) and secondary ion mass spectrometry (SIMS) depth profiling and X-ray photoelectron spectroscopy (XPS) are used for the first time to determine the elemental composition and impurity content of pyrite films grown on device substrates. Interestingly, all FeS_2 films—regardless of their phase purity or growth substrate—show very similar electrical properties, that is, thermally activated p-type conductivity with a relatively low room-temperature resistivity (≈1 Ω cm) and low mobility. The negligible electrical impact of phase and elemental impurities suggests that in-plane transport in pyrite thin films may be dominated by robust surface effects rather than bulk properties. These CVD pyrite thin films are promising for fundamental electrical studies and for the fabrication of pyrite PV device stacks.

© 2012 WILEY-VCH Verlag GmbH & Co. KGaA, Weinheim

DOI: 10.1002/aenm.201200043

2. Experimental Section

2.1. FeS_2 Thin-Film Synthesis and Sulfur Annealing

FeS_2 thin films were grown in a homemade atmospheric-pressure hot wall chemical vapor deposition reactor consisting of two collinear single-zone 1 in. quartz tube furnaces. The upstream furnace was loaded with an alumina boat containing iron(III) acetylacetonate (≥99.9%, Aldrich) at 150 °C, while the downstream furnace was heated to 300 °C and served as the growth zone. The sulfur precursor, *tert*-butyl disulfide (97%, Aldrich) was introduced directly into the growth zone by vapor entrainment in an argon flow from a stirred bubbler held at 60 °C in an oil bath. Flow rates for the iron and sulfur precursors (150 and 350 sccm, respectively) and a separate argon stream (500 sccm) were controlled by three digital mass flow controllers (Aalborg). A plug of quartz wool placed immediately upstream of the growth furnace was used to mix the precursor vapors to achieve uniform CVD growth on substrates loaded in a row within the quartz reaction tube. Soda lime glass substrates were cleaned by acetone and isopropanol and then placed in a NOCHROMIX cleaning solution overnight, followed by a DI water rinse. Molybdenum-coated glass, silicon, and quartz substrates were sonicated in acetone and isopropanol and then dried with ultra-high-purity nitrogen. The molybdenum layers were deposited by sputtering. All FeS_2 films were grown using these procedures and parameters.

Sulfur annealing was performed in 14 mm inner diameter quartz ampoules loaded with a film and a predetermined mass of solid elemental sulfur (99.999%, Alfa Aesar). Loaded ampoules were evacuated and purged with 99.999% argon three times and then evacuated to <20 mTorr and flame sealed with an oxygen-hydrogen torch. Sealed ampoules were placed in a programmable box furnace set to ramp to the desired temperature in one hour and dwell at that temperature for 2–8 h before cooling down naturally. Ampoules were placed in the furnace such that bulk sulfur would not condense on the films upon cooling.

2.2. Film Characterization

Powder X-ray diffraction (XRD) data were collected with a Rigaku Ultima III diffractometer using Cu Kα radiation and a 1° incidence angle. Quantitative phase concentrations were established by simulating powder patterns with the Jade 7.5.1 XRD software package using the Rietveld refinement procedure. High-resolution synchrotron XRD was carried out on beamline 11-BM of the Advanced Photon Source at Argonne National Laboratory. SEM imaging employed an FEI Quanta 3D FEG operating at 10 kV. Prior to SEM imaging, samples on insulating substrates were coated with ≈1 nm of Au/Pd using a Polaron SC 7620 sputterer. A Renishaw inVia confocal Raman Microscope with less than 5 mW of 532 nm laser excitation and a 50X objective lens was used for Raman experiments. Film surface roughness was measured on an Asylum MFP-3D-SA atomic force microscope. UV–vis optical absorption measurements were performed with a PerkinElmer Lambda 950 spectrophotometer equipped with a 65 mm integrating sphere. Temperature-dependent resistivity and Hall effect data were acquired on an Ecopia HMS 5000 system using the van der Pauw method with a current of 2 μA. Ohmic contacts were made by evaporating 250 nm of Ag through a shadow mask in a glovebox thermal evaporator at a pressure of 10^{-6} Torr. Qualitative thermopower measurements were carried out in a glovebox using a hotplate to establish an 80 K temperature gradient across the samples and a Keithley 2636 SourceMeter to determine the majority carrier type. Magnetic susceptibility was measured in Quantum Design MPMS-XL sample magnetometer with a SQUID detector in fields up to 1 Tesla.

XPS measurements were performed with an ESCALAB MKII surface analysis instrument (VG Scientific). The ultrahigh vacuum multichamber system was equipped with a twin anode X-ray source (Mg/Al) and a 150 mm hemispherical electron energy analyzer. Spectra presented in this study were collected using Al Kα X-rays (1486.6 eV) in constant energy mode with pass energies of 100 and 20 eV for survey scans and narrow scans, respectively. Binding energies were charge corrected by using Au foil to calibrate with respect to the Au 4f peak at 84.0 eV.

SIMS was performed by Evans Analytical Group on a Cameca dynamic SIMS instrument using 14.5 keV Cs ions for anions (S, O, H, C, Si, and Cl) and 8 keV O_2 ions for cations (Na, K, Mg, Ca, Al, and Mo). Estimated detection limits were 1×10^{15} atoms per cm^3 for Na, K, Al, Mg, and Ca, 5×10^{17} atoms per cm^3 for C, 2×10^{18} atoms per cm^3 for O and H, and 5×10^{16} atoms per cm^3 for Si and Cl. Atomic concentrations are accurate to within a factor of 2 or 3 for O, Na, K, Mg, and Ca and a factor of 10 for the other elements. The depth scale was quantified by measuring the analysis craters with a stylus profilometer and confirmed by SEM imaging of the sectioned films.

Auger electron spectroscopic measurements were performed using a modified Physical Electronics Model 670 field emission scanning Auger microprobe that has been described previously.[66] For depth profiling experiments a 5 kV, 20 nA primary electron beam was used in conjunction with a 3 kV Ar^+ ion beam. Samples were rotated at 1 rpm during sputtering and data acquisition. Direct spectra were numerically smoothed and differentiated using the Savitsky–Golay algorithm.[67] Elemental intensities were corrected by literature sensitivity factors for our instrument and the atomic concentration results were normalized to 100%.

RBS was performed by Evans Analytical Group with 2.275 MeV alpha particles incident normal to the samples and detected at backscattering angles of 160° and 100°. The samples were too rough to allow high-precision quantification with RBS. The estimated quantification uncertainty was ±3 at% for films on glass. Light elements (e.g., C and O) and cations in the glass were largely obscured by the film roughness.

3. Results and Discussion

Scanning electron microscopy (SEM) and XRD characterization of a representative 350 ± 50 nm thick FeS_2 film grown on a glass substrate by AP-CVD at 300 °C are shown in **Figure 1**. As-grown films have a highly angular, fractal-like grain morphology and consist of pyrite contaminated with a slight

© 2012 WILEY-VCH Verlag GmbH & Co. KGaA, Weinheim

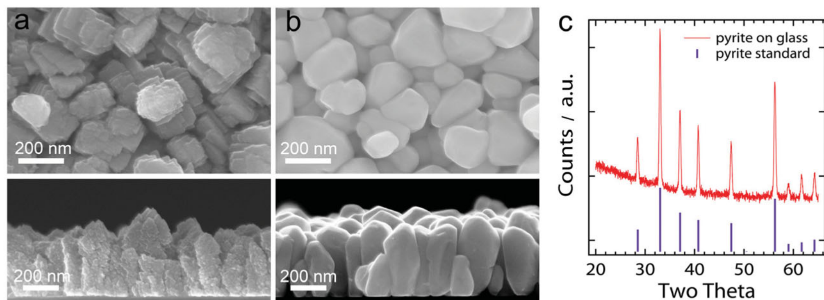

Figure 1. FeS_2 thin films on soda lime glass substrates. Plane view and cross-sectional SEM images of a film a) before and b) after sulfur annealing (0.65 atm of sulfur vapor at 500 °C for 8 h). c) XRD pattern of the sulfur-annealed film, along with a pyrite powder reference pattern. See Figure S2 in the Supporting Information for high-resolution XRD scans of an FeS_2 film before and after sulfur annealing.

marcasite (orthorhombic FeS_2) phase impurity (Figure 1a and Figure S1,S2 in the Supporting Information). Using XRD phase quantification analysis (see Experimental Section), we estimate that 350 nm thick as-grown films are ≈5% marcasite by volume. No sulfur-deficient phases (e.g., pyrrhotite $Fe_{1-x}S$) were observed in ultraslow (0.02° per minute) XRD scans using a laboratory diffractometer. Anaerobic annealing in sulfur vapor at 500–550 °C for several hours in a quartz ampoule eliminates the marcasite impurity and results in phase-pure pyrite films consisting of smooth, well-connected columnar grains 100–300 nm in lateral diameter spanning the 375 ± 50 nm thickness of the films (Figure 1b,c). The annealed films are optically flat and have a mirror-like, golden luster. The annealed films were confirmed to be phase-pure pyrite by synchrotron-based, high-resolution powder XRD using beamline 11-BM of the Advanced Photon Source at Argonne National Laboratory (Figure S3, Supporting Information), Raman spectroscopy (to check for trace marcasite) and preliminary SQUID-based magnetic susceptibility measurements of powders scraped from these films (to check for sulfur-deficient phases, most of which are magnetic).

We also grew pyrite films on Mo-coated glass substrates to make absorber layers appropriate for thin-film pyrite solar cells. **Figure 2** shows SEM and XRD data for a representative 280 ± 50 nm thick FeS_2 film on a Mo-coated glass substrate at 300 °C (400 nm thick Mo layer). As-grown films consist of pyrite contaminated with a large amount of marcasite (e.g., 45% marcasite for a 280 nm thick film). The marcasite content of as-grown films is much larger on Mo-coated glass than on plain glass because of the lower concentration of sodium on the surface of the Mo layer (vide infra). Anaerobic sulfur annealing at 500–550 °C converts the marcasite to pyrite and results in phase-pure pyrite films consisting of well-connected equiaxed grains 50–300 nm in diameter (Figure 2b,c). Similar to the films on glass, the annealed films on Mo-coated glass are optically flat and have a mirror-like, golden luster. As with the films on plain glass, no sulfur-deficient phases (e.g., pyrrhotite $Fe_{1-x}S$) were observed in ultraslow XRD scans either before or after sulfur annealing. The annealed films were also confirmed to be free of marcasite by Raman spectroscopy (**Figure 3**). Magnetic susceptibility measurements of these films were not performed due to potential complications stemming from the paramagnetism of molybdenum. The annealed pyrite films are optically flat, mechanically robust (i.e., they pass the Scotch tape adhesion test), and free of peeled regions, cracks, and pinholes.

Sulfurization causes substantial morphological and chemical changes to the underlying Mo layer of films grown on Mo-coated glass substrates, resulting in a substantial increase in the volume of the Mo coating and the appearance of two distinct layers in cross-sectional SEM images (see Figure 2b). Sulfur annealing of plain Mo-coated glass substrates (without FeS_2 films) causes similar changes (Figure S6, Supporting Information). XRD shows that the sulfur-annealed substrates consist of a mixture of MoS_2 and Mo phases (Figure S6, Supporting Information). Scanning AES depth profiles were used to determine the elemental composition of each layer in the annealed substrates (Figure S7, Supporting Information). These measurements show that sulfurization produces stratified films that can be described as MoS_2/MoS_x/Mo/MoO_x/glass with a relatively sharp MoS_x–Mo interface visible in SEM images. SIMS depth profiles of sulfur-annealed pyrite films on Mo-coated glass substrates verify the existence of a MoS_x/Mo double layer as well as the presence of MoO_x near the glass surface (see below). Despite these drastic morphological changes, sulfur annealing only slightly increases the sheet resistance of the plain substrates (from 0.35–0.44 Ω/□ to 0.8–1.5 Ω/□) and the annealed substrates still

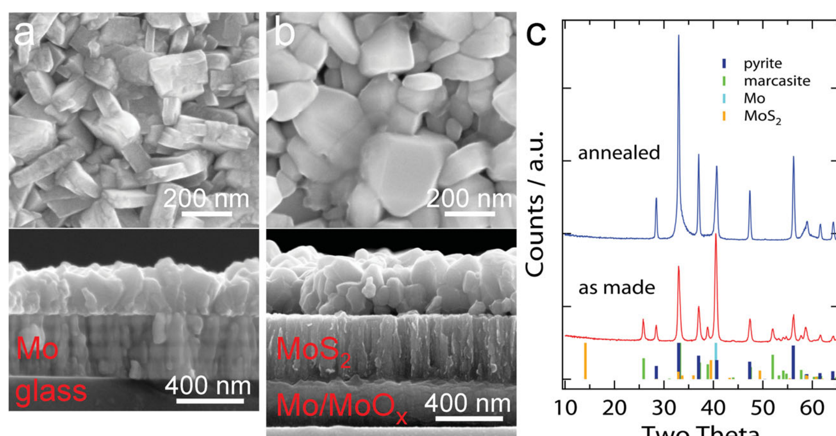

Figure 2. FeS_2 thin films on Mo-coated soda lime glass substrates. Plane view and cross-sectional SEM images of a film a) before and b) after sulfur annealing (0.65 atm of sulfur vapor at 500 °C for 2 h). c) XRD pattern of the films, along with pyrite, marcasite, molybdenum, and MoS_2 reference patterns. See Figure S4 (Supporting Information) for high-resolution XRD scans of the annealed film. Figure S5 (Supporting Information) shows SEM and XRD data for a similar film on a silicon substrate.

© 2012 WILEY-VCH Verlag GmbH & Co. KGaA, Weinheim
Adv. Energy Mater. 2012, DOI: 10.1002/aenm.201200043

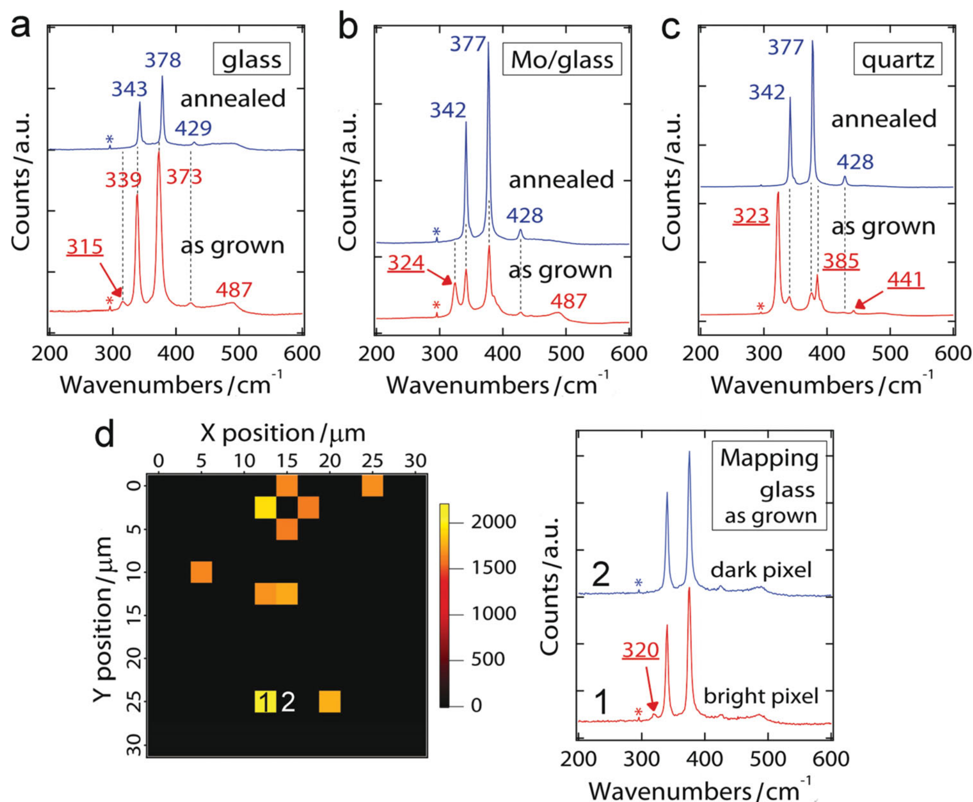

Figure 3. Phase composition by scanning Raman spectroscopy. Raman spectra of FeS_2 films on a) glass, b) Mo-coated glass, and c) quartz substrates before and after sulfur annealing ($\lambda_{incident}$ = 532 nm). Peaks due to marcasite have underlined wavenumber labels. As-grown films on quartz show the largest marcasite fraction and clearest Raman bands (at 323, 385, 391, and 441 cm^{-1}). Annealing completely eliminates marcasite in all cases. The small peak at 295 cm^{-1} labeled with an asterisk is an instrument artifact. The origin of the broad feature at 487 cm^{-1} is unknown. d) A 32.5 × 32.5 µm Raman map of the marcasite distribution (integrated 323 cm^{-1} band) for an as-grown film on glass. At right are spectra collected from adjacent bright and dark pixels ("1" and "2" on the map).

pass the tape adhesion test. Therefore, sulfur-annealed pyrite films on Mo-coated glass substrates seem suitable for the fabrication of thin-film pyrite solar cells.

The phase purity of the annealed pyrite films was characterized with Raman spectroscopy, which we found to be a substantially more sensitive technique than XRD for detecting trace marcasite impurities in pyrite. During the course of this study, several as-grown samples that appeared to be phase-pure pyrite by slow XRD scans in our laboratory diffractometer showed a clear marcasite impurity peak at 323 cm^{-1} in Raman spectra. It is possible that the marcasite domains in nearly pure pyrite films are simply too small (<1–2 nm) to efficiently diffract X-rays, and thereby evade XRD detection. The implications are troubling because most published studies of pyrite thin films rely solely on low signal-to-noise XRD data for phase characterization and do not utilize Raman spectroscopy for marcasite detection. As a result, it is likely that some of the published reports of "pyrite" actually employed mixed-phase samples contaminated to different degrees with marcasite (and perhaps also pyrrhotite and other sulfur-deficient phases).[11] In our experience, rigorous phase characterization of pyrite requires multiple high-sensitivity techniques such as Raman spectroscopy for marcasite detection and magnetic susceptibility measurements[55] or Mössbauer spectroscopy[68] for detection of pyrrhotite and other phases with compositions close to FeS (Raman spectroscopy is not suitable for trace pyrrhotite detection because pyrrhotite is Raman inactive).[69]

Figure 3 shows Raman spectra for films on glass, Mo-coated glass, and quartz substrates both before and after sulfur annealing. Before annealing, all of the films consist of a mixture of pyrite and marcasite phases, with the marcasite fraction smallest on glass and largest on quartz due to the difference in the sodium content of these substrates (see below). We observed a total of four separate Raman bands from pyrite: dominant bands at ≈343 cm^{-1} and ≈379 cm^{-1}, a small shoulder at ≈350 cm^{-1}, and a minor band at ≈429 cm^{-1}, corresponding to the A_g (S_2 dumbbell libration), E_g (S_2 dumbbell stretching), $T_g(1)$, and $T_g(3)$ vibrational modes, respectively. A fifth band expected at ≈377 cm^{-1} (the $T_g(2)$ mode) is probably present but buried within the dominant E_g peak. For marcasite, we also observed a total of four distinct Raman bands, including dominant bands at 315–324 cm^{-1} and ≈385 cm^{-1}, a shoulder at ≈391 cm^{-1}, and a minor band at ≈441 cm^{-1} (marcasite bands are denoted in Figure 3 by underlined labels). These spectra are in good agreement with previous reports.[70–72] As-grown films on glass have the lowest marcasite fraction (<5% by volume, as determined by XRD phase quantification) and typically show only a single marcasite Raman band at 315–324 cm^{-1} (Figure 3a; note that the

© 2012 WILEY-VCH Verlag GmbH & Co. KGaA, Weinheim

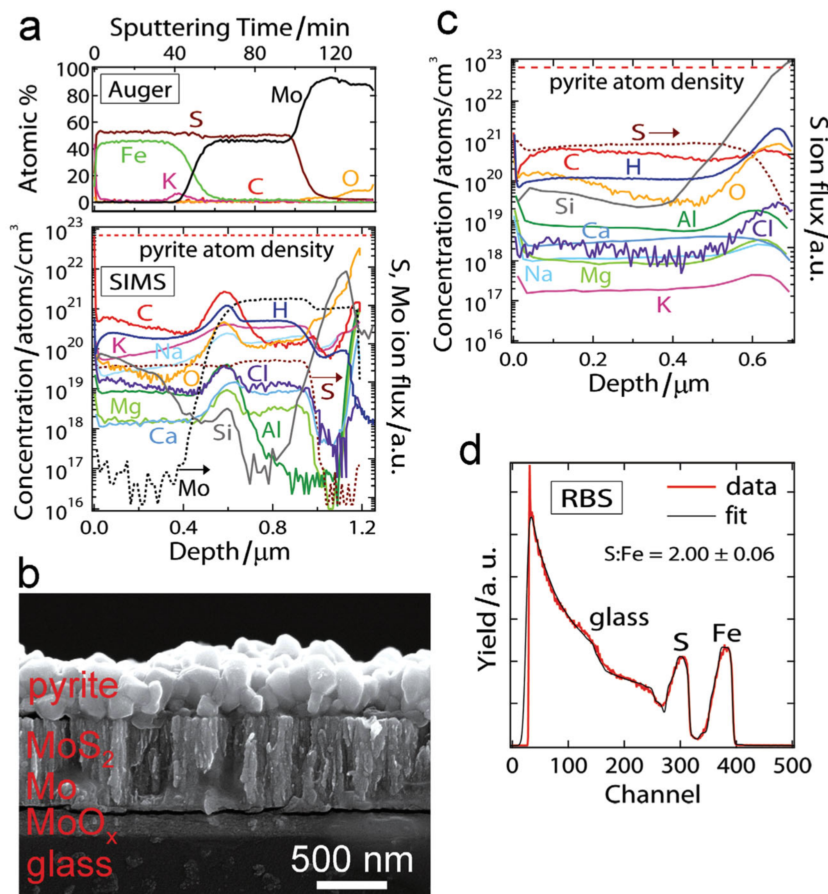

Figure 4. Bulk elemental composition of pyrite films. a) AES and SIMS depth profiles of a 450 nm thick annealed (pure pyrite) film on a Mo-coated glass substrate. The sample can be described as $FeS_2/MoS_2/MoS_x/Mo/MoO_x$/glass. The AES profile shows the presence of potassium at the pyrite surface and the FeS_2–MoS_2 interface. The relatively small sulfur signal is due to preferential sputtering of sulfur from the film. Sodium and carbon were also detected at the pyrite surface. All other elements were below AES detection limits. C, H, O, Na, K, Al, Mg, Ca, Si, and Cl were measured by SIMS (atomic concentrations plotted on the left axis). Raw ion fluxes for the matrix elements S and Mo are shown with dashed traces (right axis). The dashed red line is the pyrite bulk atomic density (7.5×10^{22} atoms cm^{-3}). b) Cross-sectional SEM image of the sample. c) SIMS depth profile for a 500 nm thick pyrite film on a silicon substrate. All impurity elements fell to their detection limits (DLs) with sputtering into the silicon substrate (typical DLs: Na, K, Al, Mg, Ca: 1×10^{15}; C: 5×10^{17}; O, H: 2×10^{18}; Si, Cl: 5×10^{16} atoms cm^{-3}). A comparison of the two SIMS profiles can be used to deduce the origin of the various impurities (see text). d) Rutherford backscattering spectrometry (RBS) profile of a 260 nm thick annealed pyrite film on a glass substrate. According to the RBS modeling fit, the stoichiometry of the film is $FeS_{2.00 \pm 0.06}$.

position of this peak shows some sample-to-sample variability). Films grown on Mo-coated glass substrates have 5–10 times more marcasite (as evidenced by both XRD and Raman) and usually show both the 385 cm^{-1} and low-energy Raman bands (Figure 3b). FeS_2 films grown on quartz substrates consist of up to ≈85% marcasite (depending on film thickness, with thicker films having more marcasite) and clearly show all four marcasite Raman bands (Figure 3c). Two-dimensional Raman maps of 250 nm thick, as-grown films on glass substrates acquired at 2.5 µm step size reveal that the marcasite impurity is distributed inhomogeneously in the samples (Figure 3d). It is likely that individual marcasite grains are scattered within the films. Sulfur annealing completely eliminates all traces of marcasite in Raman spectra and XRD patterns regardless of the initial marcasite content of the samples. Raman spectra were acquired using long signal integrations at relatively low laser irradiance (to prevent oxidation) with two different laser wavelengths (532 and 785 nm), and no marcasite was observed in the annealed films using any combination of experimental conditions. Raman maps of the annealed films show only homogeneous pyrite signal with no sign of marcasite or other phases (maps not shown). On the basis of our Raman, XRD, and initial magnetic characterization data, we are confident that the annealed CVD films are 100% pure pyrite within the detection limits of these three techniques.

AES and SIMS depth profiles were employed to elucidate the bulk elemental composition of the annealed pyrite films with ppm–ppb sensitivity. **Figure 4**a shows AES and SIMS profiles for a 450 nm thick pyrite film on a Mo-coated glass substrate (cross-sectional SEM image shown in Figure 4b). The AES atomic concentration profile indicates that the sample can be described as $FeS_2/MoS_2/MoS_x/Mo/MoO_x$/glass. AES also detected (i) a small amount of iron diffused into the MoS_2/MoS_x layers; (ii) a substantial amount of potassium at the surface of the pyrite film and a smaller accumulation of potassium at the pyrite–MoS_2 interface; (iii) sodium and carbon only at the surface of the pyrite film (Na trace not included in Figure 4a). All other elements were below AES detection limits (≈0.1 at%). The SIMS profile in Figure 4a shows the concentration of C, H, O, Na, K, Al, Mg, Ca, Si, and Cl as a function of depth into the film stack. These elements were selected as likely impurities stemming from either the CVD precursors/processing (C, H, O, Al, Si, Mg, Ca, and Cl) or the glass substrate (Na, K, Mg, Ca, and Si). Raw ion counts for two matrix elements (S and Mo) are also plotted to track position within the film stack. The S and Mo traces corroborate the general structural features of the AES data. We find the major contaminants in the pyrite film to be carbon (average of ≈0.4 at% in the FeS_2 layer), hydrogen (≈0.25 at%), potassium (≈0.1 at%), sodium (≈0.04 at%), oxygen (≈0.04 at%), and silicon (≈0.03 at%), followed by Cl (150 ppm), Al (100 ppm), and Mg and Ca (20 ppm), with estimated uncertainties of a factor of 2 to 3 for O, Na, K, Mg, and Ca, and a factor of 10 for C, H, Al, Si, and Cl. More precise concentration values will require the development of pyrite SIMS standards using high-purity synthetic single crystals. There is also a small peak in the concentrations of all impurities at the pyrite–MoS_2 interface.

© 2012 WILEY-VCH Verlag GmbH & Co. KGaA, Weinheim

DOI: 10.1002/aenm.201200043

To determine the origin of the various impurities in the pyrite film on Mo-coated glass, we compare the SIMS depth profile of this film with similar SIMS data for a 500 nm thick annealed film on an intrinsic silicon substrate (Figure 4c). Because the *i*-Si substrate is extremely pure, even by SIMS standards, it cannot be a source of any impurity other than Si itself. Indeed, the concentrations of all impurities fell below their SIMS detection limits after sputtering through the pyrite layer and several hundred nanometers into the Si substrate (not shown in Figure 4c). Of the elements monitored with SIMS, we find that only Na and K are present in significantly higher concentrations in the FeS_2 film on Mo-coated glass and have positive slopes to their depth profiles, consistent with Na and K entering the pyrite layer mainly via diffusion from the glass substrate. Alkali leaching from glass is a well-known and often useful phenomenon in thin-film PV device fabrication.[73] We find that all of the other elements (C, H, O, Al, Ca, Mg, Si, and Cl) are present at very similar concentrations in the pyrite layers of both samples, indicating that these impurities originate from the CVD chemistry/processing rather than the substrate. C, H, and O almost certainly come from the $Fe(acac)_3$ and TBDS precursors and, if so, may be an unavoidable legacy of the chemistry used to make the films. In contrast, aluminum, calcium, and magnesium are known impurities in our $Fe(acac)_3$ (at 238 ppm, 31 ppm, and 1.5 ppm, respectively) and can probably be minimized if necessary by using high-purity (99.999%) precursors. Silicon may also be an impurity in the $Fe(acac)_3$ but is not listed as such in the certificate of analysis from the manufacturer. The next most likely source of silicon is the quartzware used in the CVD and annealing furnaces. Diffusion of silicon from the substrate cannot be completely ruled out but is inconsistent with the negative slopes of the Si depth profiles in both samples. The origin of the chlorine impurity is currently unknown. We note in passing that the SIMS data do not reveal whether these impurities are in the pyrite lattice or concentrated at the surfaces and grain boundaries of the films. In addition, many other elements are undoubtedly present in the pyrite layers at concentrations that could affect the electronic properties of these films. Future work will be directed at minimizing the load of electronically active impurities as a prerequisite for achieving rational control of the electronic characteristics of pyrite thin films.

We used Rutherford backscattering spectrometry (RBS) to determine the S:Fe ratio of a typical sulfur-annealed pyrite film on a glass substrate (Figure 4d). While RBS is in principle capable of determining the stoichiometry of thin films to ≈1 at% accuracy (ideal case), our samples were too rough to allow such high-precision quantification with RBS. A fit of the data yields a stoichiometry of $FeS_{2.00 \pm 0.06}$ (i.e., 3 at% uncertainty) for this film.

XPS was used to determine the elemental composition of the surface of the annealed pyrite films. **Figure 5** presents Fe 2p, S 2p, Na 1s, O 1s, and C 1s spectra of representative pyrite films on glass and Mo-coated glass substrates. Only these five elements were detected in XPS survey scans. The Fe and S spectra of both films are consistent with nearly oxide-free FeS_2 surfaces. Oxygen spectra show weak signatures of at least two oxygen species on each film (binding energies of 531.4 and 533.3 eV on glass, 532.2 and 534.8 eV on Mo-coated glass), which indicate

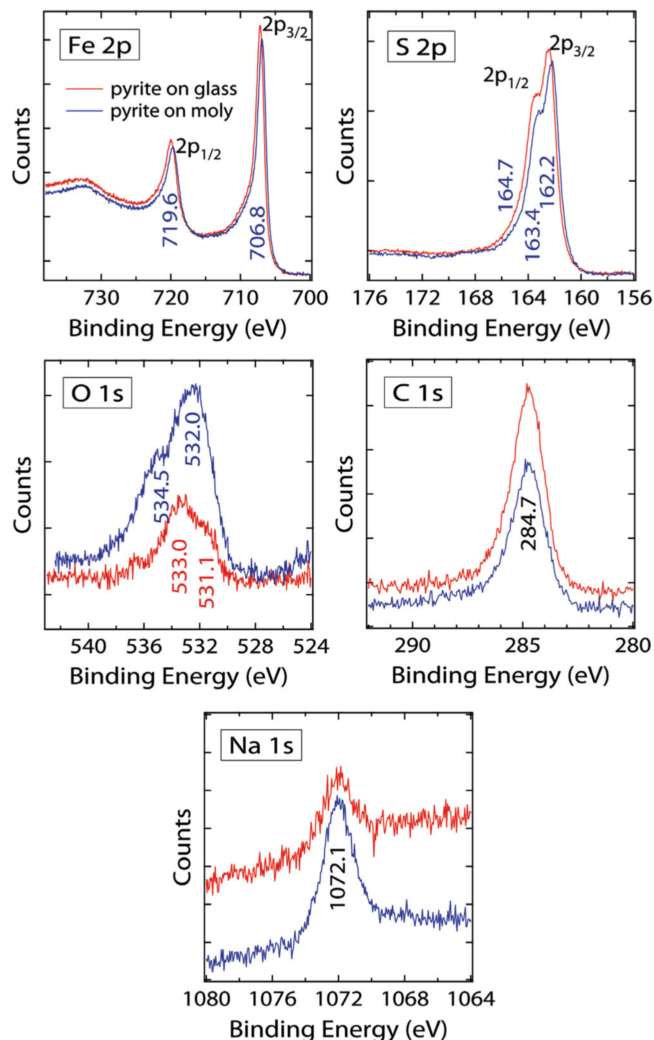

Figure 5. Surface composition. XPS spectra of sulfur-annealed pyrite films on glass and Mo-coated glass substrates. Samples were annealed in elemental sulfur at 500 °C for 6 h or 2 h, respectively, and confirmed to be pure pyrite within the sensitivity of XRD. Both films were exposed to air for ≈1 min as they were introduced into the XPS chamber. Film thicknesses: 250 nm.

the presence of small amount of oxidized iron and/or sulfur that is not easily detected in Fe and S spectra. The slight sulfur shoulder at 165.0 eV may result from elemental sulfur on the film surface (ostensibly from the sulfur annealing). The sodium detected on each film at 1072.4 eV is assigned to Na_2S or Na_2O[74] and was readily removed by either brief argon sputtering or by rinsing with water,[75] suggesting that sodium is present *on* rather than *in* the pyrite grains, which is typical of alkali leaching from glass into polycrystalline chalcogenide thin films.[76] A comprehensive discussion of the synchrotron-based XPS characterization of these films will be published shortly.[75]

The optical absorption coefficient and bandgap of sulfur-annealed pyrite films were determined from transmittance and reflectance measurements using an integrating sphere (**Figure 6**). The absorption coefficient (α) reaches a value of 5×10^4 cm^{-1} at $h\nu = 1.25$ eV ($\alpha^{-1} = 200$ nm) and $>3 \times 10^5$ cm^{-1} for

© 2012 WILEY-VCH Verlag GmbH & Co. KGaA, Weinheim

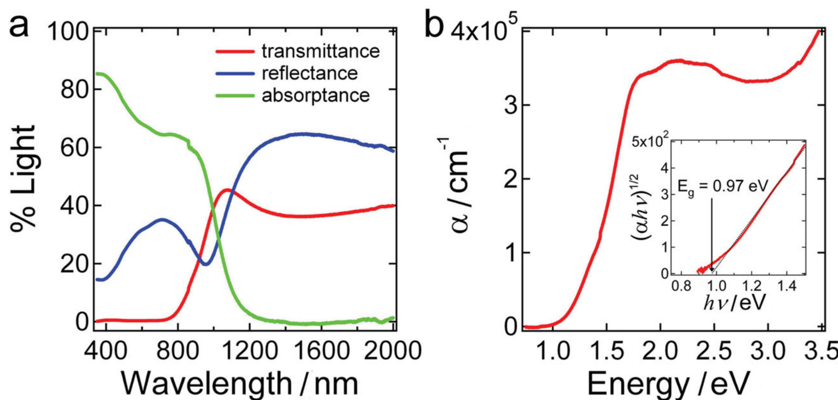

Figure 6. Optical properties. (a) Transmittance, reflectance, and absorptance of a representative 150 nm thick pyrite film on a glass substrate measured by integrating sphere UV–vis spectroscopy. (b) Calculated absorption coefficient α across the solar spectrum (0.5–3.5 eV). α might be underestimated by up to 20% due to possible void spaces within the film. Inset is a plot of $(\alpha h\nu)^{1/2}$ versus $h\nu$ showing an estimated allowed indirect bandgap of 0.97 ± 0.05 eV. This sample was sulfur annealed at 500 °C for 2 h.

$h\nu > 1.7$ eV ($\alpha^{-1} < 33$ nm). The bandgap fits best as an allowed indirect transition with $E_g = 0.97 \pm 0.05$ eV, in good agreement with the most commonly cited bandgap value for pyrite ($E_g \approx 0.95$ eV).[13] Any subgap optical absorption that may be present is below the detection limit of our transmittance/reflectance measurement (<500 cm^{-1}) and will require a more sensitive technique, such as photothermal deflection spectroscopy (PDS), for accurate quantification.

The electrical properties of FeS_2 films on glass and quartz substrates were assessed by variable-temperature Hall effect measurements (90–300 K) in a van der Pauw geometry with thermally deposited, ohmic silver contacts. The dark resistivity of pure pyrite films was 1.5 ± 0.5 Ω cm at room temperature and 30 ± 5 Ω cm at 90 K (red trace in **Figure 7**). We found no difference between pure pyrite films made on glass and quartz substrates. Arrhenius plots of the resistivity were quasilinear with a small activation energy of 28.8 ± 1.8 meV (Figure 7, inset). The temperature dependence of the resistivity is characteristic of a highly doped but non-degenerate semiconductor. The in-plane Hall mobility of these films was too low to be measured (<1 cm^2 V^{-1} s^{-1}), which also prevented determination of the carrier type from the sign of the Hall voltage. However, qualitative thermopower measurements always indicated that the films were *p*-type. The fact that these general features—low resistivity, low mobility, and *p*-type transport—have been reported for nearly all unintentionally doped pyrite thin films regardless of fabrication method may imply that transport in polycrystalline pyrite films is governed by surface/interface effects rather than bulk properties (vide infra).

Surprisingly, we find the electrical properties of mixed-phase pyrite/marcasite films to be nearly identical to the pure-phase pyrite films. The room-temperature resistivity of the mixed-phase (blue trace in Figure 7) films is only ≈5 times smaller, while the activation energies differ by less than 10% from the pure pyrite values (red trace in Figure 7). Furthermore, the behavior of mixed-phase films on glass and quartz substrates is indistinguishable. The insensitivity of FeS_2 electrical properties to both bulk phase impurities and substrate-derived elemental impurities is further evidence that charge transport in polycrystalline pyrite films is controlled by surface effects, for example, a conductive inversion layer, that is quite insensitive to variations in bulk composition.

Our electrical results are in good agreement with literature. Unintentionally doped polycrystalline pyrite thin films are always reported to be *p*-type by in-plane thermopower and (less frequently, due to the low carrier mobility) Hall measurements and feature a narrow range of low resistivity (0.5–10 Ω cm), high carrier concentration (10^{18}–10^{20} cm^{-3}), and low mobility (<2 cm^2 V^{-1} s^{-1}) regardless of the preparation method and S:Fe stoichiometry.[52,77] This is true of purportedly sulfur-deficient[35,38,52,55,65] and iron-deficient[35,51,52,55,65] films made by CVD, sputtering,[38,39] sulfurization of iron films,[34,35,37] and molecular beam epitaxy.[47] In other words, pyrite thin-film electrical properties appear to be independent of S:Fe stoichiometry, which implies that the native defects commonly expected to act as donors and

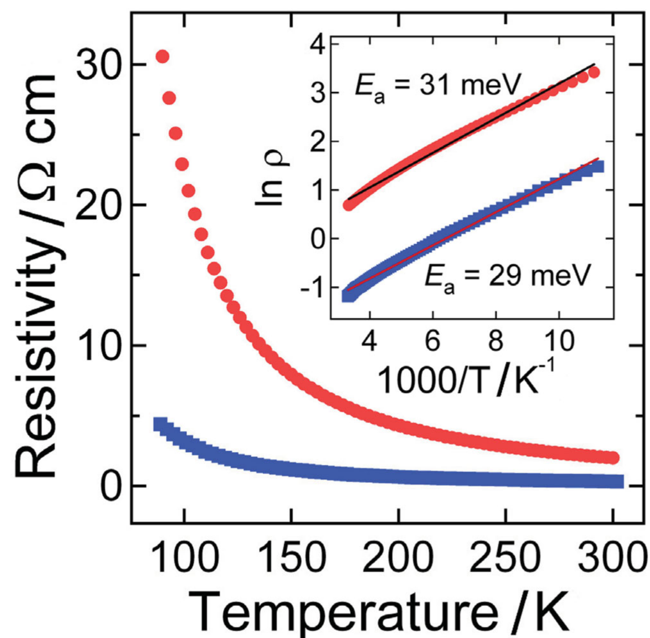

Figure 7. Electrical resistivity of pure pyrite and mixed-phase FeS_2 films. Resistivity as a function of temperature (90–300 K) for a representative 200 nm thick annealed film on a glass substrate (pure pyrite, red circles) and a 300 nm thick mixed-phase film on a quartz substrate (45% marcasite, blue squares). Six annealed films and three mixed-phase films were measured in the van der Pauw geometry with ohmic Ag contacts. The room-temperature resistivity of pyrite films (on either glass or quartz substrates) is 1.5 ± 0.5 Ω cm, while that of mixed-phase films on quartz is 0.30–0.35 Ω cm. Inset is an Arrhenius plot of the data showing quasilinear behavior and very similar activation energies for the pyrite and mixed-phase films (E_a = 31 meV and 29 meV, respectively). These values were very reproducible across samples prepared and measured on different days (E_a = 28.8 ± 1.8 meV for pyrite films and 26.8 ± 1.1 meV for mixed-phase films).

© 2012 WILEY-VCH Verlag GmbH & Co. KGaA, Weinheim
Adv. Energy Mater. 2012, DOI: 10.1002/aenm.201200043

acceptors (sulfur and iron vacancies, respectively) do not dominate the electrical behavior of pyrite films. Calculations by several groups show that native defects should exist only at negligible concentrations in bulk pyrite and cannot account for the large carrier densities observed.[19,64,78,79] However, native defects may be present in high concentration near the surface, where defect formation energies are lower due in part to easier steric relaxation. We note that these calculations support the notion that bulk pyrite is a stoichiometric line compound. This follows an earlier review of the experimental literature by Ellmer and Hopfner, who concluded that pyrite is probably a stoichiometric compound with a S:Fe ratio of 2.00 and a maximum vacancy concentration of several parts per thousand ($<10^{19}$ cm^{-3}).[80] Most measured S:Fe ratios for natural and synthetic pyrite crystals and properly prepared pyrite thin films support a $FeS_{2.00}$ stoichiometry within the error of the measurements. If pyrite is in fact a line compound, as seems likely, then deviations from S:Fe = 2.00 can probably be explained by sulfur-deficient phase impurities or measurement errors in the case of sulfur deficiency and by sulfur accumulation at grain boundaries in the case of sulfur excess. We see no convincing link between the reported S:Fe ratio and the electronic properties of pyrite thin films. Only by intentional doping with donors such as Cl, Br, or Co have *n*-type polycrystalline pyrite thin films been made.[56,57]

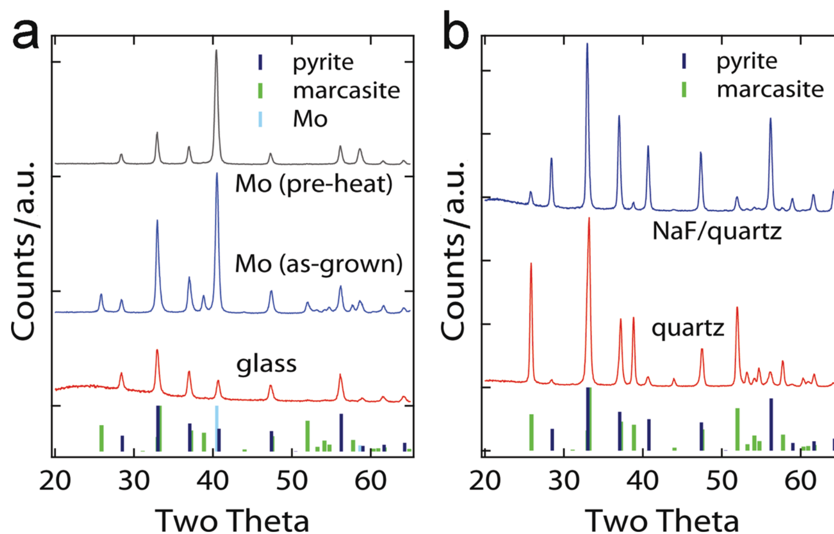

Figure 8. Effect of Na on the phase composition of FeS_2 films. a) XRD patterns of films grown on soda lime glass and Mo-coated glass substrates with and without a thermal pretreatment prior to CVD growth. (b) XRD patterns of films grown on quartz and NaF-coated quartz substrates. In all cases, greater Na availability favors pyrite over marcasite.

There are at least three credible explanations for the ubiquitous electrical behavior of nominally undoped pyrite thin films: phase impurities, accidental oxygen doping, and surface effects. First, pyrite samples may inevitably (due to thermodynamic considerations) contain nanoscale inclusions of metallic, sulfur-deficient phases. This idea, advocated recently by Yu et al.,[19] seems at odds with the experimental evidence, particularly the very high external quantum efficiency of pyrite photoelectrochemical[10] and Schottky[16,81] solar cells and sensitive magnetic measurements that show no evidence of pyrrhotite or other magnetic sulfur-deficient phases above ppm levels in properly prepared pyrite films.[55] A second possibility is that all pyrite films are contaminated with oxygen and that oxygen acts as an efficient acceptor to produce highly-doped, *p*-type films. Sun et al.[79] has argued that pyrite synthesized in iron-rich, oxidizing conditions may be contaminated with substitutional oxygen (O_S defects) at a concentration of $\approx 10^{19}$ cm^{-3} and that O_S impurities are *p*-type dopants. Concern over oxygen is reasonable given the potential for oxygen incorporation in pyrite films made by different methods. It is also consistent with the substantial oxygen concentration [$O(10^{19}$ $cm^{-3})$] measured in our films by SIMS (Figure 4). However, many pyrite film syntheses utilize highly reducing, nearly oxygen-free (ppm O_2) conditions that would be expected to produce films with very low bulk oxygen concentrations. Moreover, our own density functional theory calculations show that O_S is neither an acceptor nor a donor in bulk pyrite.[64] The viability of the O_S hypothesis should be carefully evaluated in future experimental studies.

Surface effects provide a third explanation for the universal electrical behavior of nominally undoped pyrite films. As argued by Tributsch and co-workers[52] almost 20 years ago, the similarity of the electrical characteristics regardless of stoichiometry and preparation method suggests that the electrical behavior of pyrite thin films is not determined by the bulk properties of the crystallites but rather by their surface properties. Surface and grain boundary effects commonly control the electrical properties of semiconductor thin films via surface nonstoichiometry, oxidation, charge-transfer doping from adsorbed species, intergrain potential barriers to transport, surface accumulation/inversion layers that make the surface region very different from the bulk, and so on.[82,83] Given the well-known lability of pyrite surfaces,[17] it is reasonable to expect that surface composition and/or electronic effects are very important for pyrite thin films and may be responsible for their measured electrical properties. We are now using pyrite films made by CVD and several solution-phase approaches to explore this premise en route to fabricating pyrite solar cells.

We now turn to the influence of sodium and sulfur on the growth and annealing of pyrite thin films. We find that the presence of sodium in the substrate strongly favors the nucleation and growth of pyrite at the expense of marcasite. To illustrate this point, **Figure 8** compares the XRD patterns of representative as-grown FeS_2 films on soda lime glass substrates (which contain ≈150 000 ppm Na_2O) and quartz substrates (≈0.7 ppm Na)[84] using identical CVD growth conditions. The film on glass ("glass" in Figure 8a) shows a much smaller marcasite impurity (≈5% by volume) than the film on quartz ("quartz" in Figure 8b; ≈85% by volume). Sodium was detected by XPS at the surface of the FeS_2 film on glass (see Figure 5). Furthermore, while films grown on Mo-coated glass substrates typically have a substantial marcasite impurity (≈45%), the

© 2012 WILEY-VCH Verlag GmbH & Co. KGaA, Weinheim

impurity is nearly eliminated (<4%) when the Mo substrates are pre-annealed in argon (500 °C, 2 h) prior to CVD growth. XPS shows that this thermal pretreatment brings sodium to the surface of the Mo film, which appears to be responsible for promoting pyrite and/or suppressing marcasite formation during CVD growth. To obtain more direct evidence for the effect of sodium, we grew FeS_2 films on quartz substrates coated with ≈3 nm of NaF by thermal evaporation. As expected, the NaF-coated quartz substrates yielded much purer pyrite films compared to quartz substrates without a NaF coating (≈17% and ≈85% marcasite, respectively; Figure 8b). We conclude that sodium leaching from Na-containing substrates is a useful way to reduce the marcasite content of as-grown FeS_2 films and to decrease the temperature and time needed to eliminate any residual marcasite via sulfur annealing. However, preheating and NaF seeding cause the surface roughness of the pyrite films to markedly increase compared to as-grown films. Only when sodium is introduced naturally via diffusion from the glass substrate is the root mean square (rms) surface roughness <10% of the film thickness. Exactly how sodium encourages pyrite growth, as well as the possible impact of sodium on the electronic properties of pyrite films, are important topics for future studies.

As shown above, a rigorously complete conversion of marcasite to pyrite can be achieved by annealing mixed-phase FeS_2 films at relatively high temperatures (>500 °C) and sulfur partial pressures. We observed appreciable marcasite-to-pyrite phase conversion only when annealing at >450 °C, in agreement with past studies[50] and consistent with the alleged metastability of marcasite.[85] Annealing above 600 °C in sulfur ambient results in excessive grain growth, surface roughening, and pinhole formation, rendering the films unsuitable for electrical and device studies, so we focused on 500–550 °C annealing treatments. We found that the rate and extent of phase conversion depends on the sulfur partial pressure in addition to the temperature, which is surprising since marcasite and pyrite have the same stoichiometry (FeS_2) and thus there is no simple reason why a sulfur overpressure should favor one phase over the other. **Figure 9** shows XRD scans of the marcasite {120} and pyrite {211} peaks of five identical, 450 nm thick, mixed-phase FeS_2 films annealed at 550 °C for 2 h in various pressures of elemental sulfur vapor. The data clearly illustrate a systematically larger pyrite peak and smaller marcasite peak with higher sulfur pressures. While we show just two reflections in Figure 9, all of the peaks in wide-angle XRD patterns followed the same trend, confirming that a higher sulfur pressure induces marcasite-to-pyrite phase conversion rather than merely changes in film texturing. However, as with excessively high temperatures, excessively high sulfur pressures cause undesirable changes to the film morphology (runaway grain growth, pinholes, dewetting, etc.), so we anneal our CVD films at 500–550 °C in moderate amounts of sulfur using fairly long times (2–8 h). We note that annealing in 1 atm of pure H_2S at temperatures up to 450 °C fails to convert marcasite to pyrite at an appreciable rate, while H_2S annealing above 450 °C results in sulfur evaporation and the appearance of pyrrhotite ($Fe_{1-x}S$) phases. Annealing above 400 °C in the absence of any source of sulfur (e.g., in pure argon) creates pyrrhotite and other sulfur-deficient compounds.

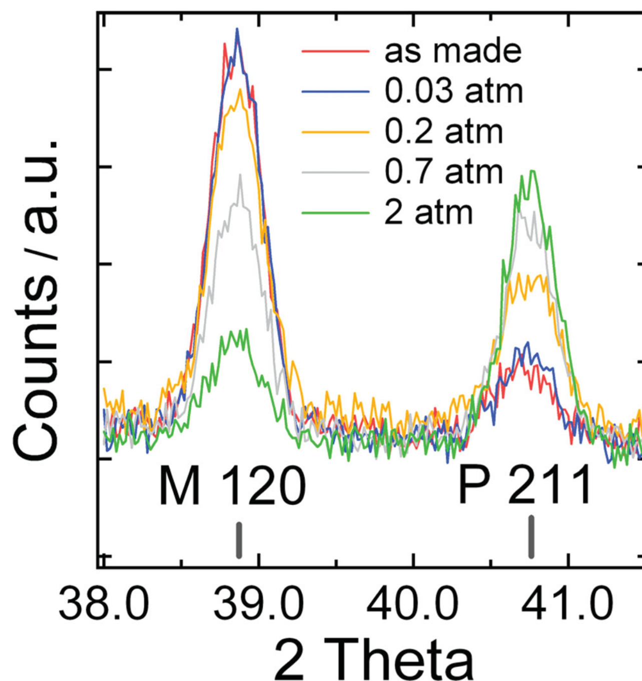

Figure 9. Effect of sulfur partial pressure on the marcasite-to-pyrite phase conversion during annealing. XRD scans (2Θ = 38.0–41.5°, showing the marcasite 120 and pyrite 211 reflections) of five identical mixed-phase FeS_2 films on quartz substrates annealed at 550 °C for 2 h in various pressures of sulfur vapor. Marcasite conversion to pyrite is more rapid and complete at larger sulfur partial pressures. (M = marcasite; P = pyrite.)

3. Conclusion

Phase-pure, polycrystalline iron pyrite thin films were deposited on glass, Mo-coated glass, and other substrates by atmospheric-pressure CVD of $Fe(acac)_3$ and *tert*-butyl disulfide at 300 °C followed by sulfur annealing at 500–550 °C, to fully convert marcasite phase impurities to pyrite. Pyrite is favored over marcasite by the presence of sodium in the substrate and by higher sulfur vapor pressures during annealing. Systematic XRD and Raman measurements and initial magnetic susceptibility results establish that the annealed films are completely pure pyrite. The films consist of large, densely packed pyrite grains and are uniform in thickness (±5%), fairly smooth (rms roughness of the order of 10% of the film thickness), free of cracks and through-film pinholes, and mechanically adherent and robust. The films have an indirect optical bandgap of 0.97 ± 0.05 eV. Their optical absorption coefficients are 5×10^4 cm^{-1} at $h\nu = 1.25$ eV and > 3 $\times 10^5$ cm^{-1} for $h\nu > 1.7$ eV. Annealed films on Mo-coated glass substrates can be described as $FeS_2/MoS_2/MoS_x/Mo/MoO_x$/glass stacks. SIMS shows that the total impurity load in the pyrite layers of these films is ≈1 at%, with all elements apart from Na and K originating from the CVD chemistry/processing rather than the substrate. The use of higher-purity precursors and alkali blocking layers under the Mo films is a promising route to lowering the concentrations of all impurities other than C, H, and O (which may be intrinsic to the CVD chemistry). However, in-plane electrical properties of the films are quite insensitive to phase and elemental purity: regardless of the

© 2012 WILEY-VCH Verlag GmbH & Co. KGaA, Weinheim
Adv. Energy Mater. 2012, DOI: 10.1002/aenm.201200043

presence of marcasite or the use of glass versus quartz as the substrate, all films show *p*-type, thermally activated transport with a small activation energy (≈30 meV), a room-temperature resistivity of ≈1 Ω cm, and a hole mobility that is too small to measure by the Hall effect. This ubiquitous electrical behavior strongly implies that surface effects dominate in-plane charge transport in polycrystalline FeS_2 films, but transport properties along the substrate normal may be very different because of the absence of grain boundaries in this direction. The CVD pyrite films described here will serve as an excellent platform for learning how to control the electrical properties of thin-film pyrite and for fabricating high-quality *p–n* heterojunctions for efficient thin-film pyrite solar cells.

Supporting Information

Supporting Information is available from the Wiley Online Library or from the author.

Acknowledgements

We thank the NSF SOLAR Program (Award CHE-1035218) for support of this work. We also thank Professor Zachary Fisk for the use of his quartz sealing setup and Tatyana Sheps for help with Raman spectroscopy. Use of the Advanced Photon Source at Argonne National Laboratory was supported by the U. S. Department of Energy, Office of Science, Office of Basic Energy Sciences, under Contract No. DE-AC02-06CH11357. C.L.P. acknowledges support by the U.S. Department of Energy under Contract No. DE-AC36-08-GO28308 with the National Renewable Energy Laboratory.

Received: January 16, 2012
Published online:

[1] P. P. Altermatt, T. Kiesewetter, K. Ellmer, H. Tributsch, *Sol. Energy Mater. Sol. Cells* **2002**, *71*, 181.
[2] A. Ennaoui, H. Tributsch, *Sol. Energy Mater.* **1986**, *14*, 461.
[3] G. Smestad, A. Ennaoui, S. Fiechter, H. Tributsch, W. K. Hofmann, M. Birkholz, W. Kautek, *Sol. Energy Mater.* **1990**, *20*, 149.
[4] C. Wadia, A. P. Alivisatos, D. M. Kammen, *Environ. Sci. Technol.* **2009**, *43*, 2072.
[5] A. Ennaoui, H. Tributsch, *Sol. Cells* **1984**, *13*, 197.
[6] V. Antonucci, A. S. Arico, N. Giordano, P. L. Antonucci, U. Russo, D. L. Cocke, F. Crea, *Sol. Cells* **1991**, *31*, 119.
[7] A. Ennaoui, S. Fiechter, H. Tributsch, M. Giersig, R. Vogel, H. Weller, *J. Electrochem. Soc.* **1992**, *139*, 2514.
[8] O. Blenk, PhD Thesis (In German), University of Konstanz (Konstanz, Germany) **1995**.
[9] A. F. Ennaoui, S. Fiechter, G. Smestad, H. Tributsch, in *World Renewable Energy Congress. Energy and the Environment* (Ed: A. A. M. Sayigh), Pergamon Press, Oxford **1990**.
[10] A. Ennaoui, S. Fiechter, W. Jaegermann, H. Tributsch, *J. Electrochem. Soc.* **1986**, *133*, 97.
[11] N. Alonso-Vante, G. Chatzitheodorou, S. Fiechter, N. Mgoduka, I. Poulios, H. Tributsch, *Sol. Energy Mater.* **1988**, *18*, 9.
[12] M. Birkholz, S. Fiechter, A. Hartmann, H. Tributsch, *Phys. Rev. B* **1991**, *43*, 11926.
[13] A. Ennaoui, S. Fiechter, C. Pettenkofer, N. Alonso-Vante, K. Büker, M. Bronold, C. Höpfner, H. Tributsch, *Sol. Energy Mater. Sol. Cells* **1993**, *29*, 289.
[14] M. Bronold, Y. Tomm, W. Jaegermann, *Surf. Sci.* **1994**, *314*, L931.
[15] M. Bronold, C. Pettenkofer, W. Jaegermann, *J. Appl. Phys.* **1994**, *76*, 5800.
[16] K. Buker, N. Alonsovante, H. Tributsch, *J. Appl. Phys.* **1992**, *72*, 5721.
[17] R. Murphy, D. R. Strongin, *Surf. Sci. Rep.* **2009**, *64*, 1.
[18] K. M. Rosso, U. Becker, M. F. Hochella, *Am. Mineral.* **1999**, *84*, 1535.
[19] L. Yu, S. Lany, R. Kykyneshi, V. Jieratum, R. Ravichandran, B. Pelatt, E. Altschul, H. A. S. Platt, J. F. Wager, D. A. Keszler, A. Zunger, *Adv. Energy Mater.* **2011**, *1*, 748.
[20] W. L. Bragg, *Proc. R. Soc. London A* **1914**, *89*, 476.
[21] E. K. Li, K. H. Johnson, D. E. Eastman, J. L. Freeouf, *Phys. Rev. Lett.* **1974**, *32*, 470.
[22] A. Fujimori, K. Mamiya, T. Mizokawa, T. Miyadai, T. Sekiguchi, H. Takahashi, N. Môri, S. Suga, *Phys. Rev. B* **1996**, *54*, 16329.
[23] H. W. Nesbitt, A. G. Berlich, S. L. Harmer, I. Uhlig, G. M. Bancroft, R. Szargan, *Am. Mineral.* **2004**, *89*, 382.
[24] J. F. W. Mosselmans, R. A. D. Pattrick, G. Laan, J. M. Charnock, D. J. Vaughan, C. M. B. Henderson, C. D. Garner, *Phys. Chem. Miner.* **1995**, *22*, 311.
[25] K. C. Prince, M. Matteucci, K. Kuepper, S. G. Chiuzbaian, S. Bartkowski, M. Neumann, *Phys. Rev. B* **2005**, *71*, 085102.
[26] T. A. Bither, R. J. Bouchard, W. H. Cloud, P. C. Donohue, W. J. Siemons, *Inorg. Chem.* **1968**, *7*, 2208.
[27] W. Folkerts, G. A. Sawatzky, C. Haas, R. A. D. Groot, F. U. Hillebrecht, *J. Phys. C: Solid State Phys.* **1987**, *20*, 4135.
[28] P. Raybaud, G. Kresse, J. Hafner, H. Toulhoat, *J. Phys.: Condens. Matter* **1997**, *9*, 11085.
[29] V. Eyert, K. H. Hock, S. Fiechter, H. Tributsch, *Phys. Rev. B* **1998**, *57*, 6350.
[30] G. U. von Oertzen, W. M. Skinner, H. W. Nesbitt, *Phys. Rev. B* **2005**, *72*, 235427.
[31] I. J. Ferrer, C. Sanchez, *J. Appl. Phys.* **1991**, *70*, 2641.
[32] C. de las Heras, J. L. M. de Vidales, I. J. Ferrer, C. Sánchez, *J. Mater. Res.* **1996**, *11*, 211.
[33] L. Meng, M. S. Liu, *Mater. Sci. Eng. B: Solid State Mater. Adv. Technol.* **1999**, *60*, 168.
[34] L. Meng, Y. H. Liu, L. Tian, *J. Cryst. Growth* **2003**, *253*, 530.
[35] D. Y. Wan, Y. T. Wang, B. Y. Wang, C. X. Ma, H. Sun, L. Wei, *J. Cryst. Growth* **2003**, *253*, 230.
[36] A. Pascual, P. Diaz-Chao, I. J. Ferrer, C. Sanchez, J. R. Ares, *Sol. Energy Mater. Sol. Cells* **2005**, *87*, 575.
[37] N. Hamdadou, A. Khelil, J. C. Bernede, *Mater. Chem. Phys.* **2003**, *78*, 591.
[38] D. Lichtenberger, K. Ellmer, R. Schieck, S. Fiechter, H. Tributsch, *Thin Solid Films* **1994**, *246*, 6.
[39] G. Willeke, R. Dasbach, B. Sailer, E. Bucher, *Thin Solid Films* **1992**, *213*, 271.
[40] M. Birkholz, D. Lichtenberger, C. Hopfner, S. Fiechter, *Sol. Energy Mater. Sol. Cells* **1992**, *27*, 243.
[41] D. Susac, L. Zhu, M. Teo, A. Sode, K. C. Wong, P. C. Wong, R. R. Parsons, D. Bizzotto, K. A. R. Mitchell, S. A. Campbell, *J. Phys. Chem. C* **2007**, *111*, 18715.
[42] C. Delasheras, I. J. Ferrer, C. Sanchez, *J. Phys.: Condens. Matter* **1994**, *6*, 10177.
[43] C. Delasheras, I. J. Ferrer, C. Sanchez, *Appl. Surf. Sci.* **1991**, *50*, 505.
[44] S. Nakamura, A. Yamamoto, *Sol. Energy Mater. Sol. Cells* **2001**, *65*, 79.
[45] E. L. Li, S. Seki, F.-B. Liu, J.-B. Zheng, *Semicond. Photon. Technol.* **2001**, *7*, 89.
[46] A. Yamamoto, M. Nakamura, A. Seki, E. L. Li, A. Hashimoto, S. Nakamura, *Sol. Energy Mater. Sol. Cells* **2003**, *75*, 451.
[47] M. Bronold, S. Kubala, C. Pettenkofer, W. Jaegermann, *Thin Solid Films* **1997**, *304*, 178.
[48] G. Chatzitheodorou, S. Fiechter, R. Könenkamp, M. Kunst, W. Jaegermann, H. Tributsch, *Mater. Res. Bull.* **1986**, *21*, 1481.

© 2012 WILEY-VCH Verlag GmbH & Co. KGaA, Weinheim

[49] D. M. Schleich, H. S. W. Chang, *J. Cryst. Growth* **1991**, *112*, 737.
[50] A. Ennaoui, S. Schroetter, S. Fiechter, H. Tributsch, *J. Mater. Sci. Lett.* **1992**, *11*, 1131.
[51] K. L. Ellmer, D. Lichtenberger, A. Ennaoui, C. Hopfner, S. Fiechter, H. Tributsch, *Proc. 23rd Photovoltaics Spec. Conf.* **1993**, p. 535.
[52] C. Hopfner, K. Ellmer, A. Ennaoui, C. Pettenkofer, S. Fiechter, H. Tributsch, *J. Cryst. Growth* **1995**, *151*, 325.
[53] B. Thomas, C. Höpfner, K. Ellmer, S. Fiechter, H. Tributsch, *J. Cryst. Growth* **1995**, *146*, 630.
[54] B. Thomas, K. Ellmer, M. Müller, C. Höpfner, S. Fiechter, H. Tributsch, *J. Cryst. Growth* **1997**, *170*, 808.
[55] B. Thomas, T. Cibik, C. Hopfner, K. Diesner, G. Ehlers, S. Fiechter, K. Ellmer, *J. Mater. Sci.: Mater. Electron.* **1998**, *9*, 61.
[56] J. Oertel, K. Ellmer, W. Bohne, J. Röhrich, H. Tributsch, *J. Cryst. Growth* **1999**, *198–199*, 1205.
[57] N. Takahashi, T. Sawada, T. Nakamura, *J. Mater. Chem.* **2000**, *10*, 2346.
[58] N. Takahashi, Y. Nakatani, T. Yatomi, T. Nakamura, *Chem. Mater.* **2003**, *15*, 1763.
[59] L. Reijnen, B. Meester, A. Goossens, J. Schoonman, *J. Electrochem. Soc.* **2000**, *147*, 1803.
[60] S. Fiechter, J. Mai, A. Ennaoui, W. Szacki, *J. Cryst. Growth* **1986**, *78*, 438.
[61] S. W. Lehner, K. S. Savage, J. C. Ayers, *J. Cryst. Growth* **2006**, *286*, 306.
[62] G. Willeke, O. Blenk, C. Kloc, E. Bucher, *J. Alloys Compd.* **1992**, *178*, 181.
[63] Y. Tomm, R. Schieck, K. Ellmer, S. Fiechter, *J. Cryst. Growth* **1995**, *146*, 271.
[64] J. Hu, Y. Zhang, M. Law, R. Wu, *Phys. Rev. B* **2012**, *85*, 085203.
[65] B. Meester, L. Reijnen, A. Goossens, J. Schoonman, *Chem. Vap. Deposition* **2000**, *6*, 121.
[66] C. L. Perkins, B. Egaas, I. Repins, B. To, *Appl. Surf. Sci.* **2010**, *257*, 878.
[67] D. Briggs, M. P. Seah, *Practical Surface Analysis*, Wiley, New York **1990**.
[68] J. A. Morice, L. V. C. Rees, D. T. Rickard, *J. Inorg. Nucl. Chem.* **1969**, *31*, 3797.
[69] T. P. Mernagh, A. G. Trudu, *Chem. Geol.* **1993**, *103*, 113.
[70] S. N. White, *Chem. Geol.* **2009**, *259*, 240.
[71] C. Sourisseau, R. Cavagnat, M. Fouassier, *J. Phys. Chem. Solids* **1991**, *52*, 537.
[72] H. Vogt, T. Chattopadhyay, H. J. Stolz, *J. Phys. Chem. Solids* **1983**, *44*, 869.
[73] K. Granath, M. Bodegård, L. Stolt, *Sol. Energy Mater. Sol. Cells* **2000**, *60*, 279.
[74] A. Barrie, F. J. Street, *J. Electron Spectrosc. Relat. Phenom.* **1975**, *7*, 1.
[75] Y. L. Ming Hsin Cheng, N. Berry, A. M. Margarella, J. C. Hemminger, M. Law, unpublished.
[76] U. Rau, K. Taretto, S. Siebentritt, *Appl. Phys. A: Mater. Sci. Process.* **2009**, *96*, 221.
[77] J. R. Ares, I. J. Ferrer, F. Cuevas, C. R. Sanchez, *Thin Solid Films* **2001**, *387*, 97.
[78] S. Fiechter, *Sol. Energy Mater. Sol. Cells* **2004**, *83*, 459.
[79] R. Sun, M. K. Y. Chan, G. Ceder, *Phys. Rev. B* **2011**, *83*, 235311.
[80] K. Ellmer, C. Hopfner, *Phil. Mag. A* **1997**, *75*, 1129.
[81] K. Buker, N. Alonsovante, R. Scheer, H. Tributsch, *Berichte Bunsengesellschaft Phys. Chem.* **1994**, *98*, 674.
[82] L. Eckertova, *Physics of Thin Films*, Springer, Berlin/New York **1986**.
[83] O. Bierwagen, S. Choi, J. S. Speck, *Phys. Rev. B* **2011**, *84*, 235302.
[84] GE 214 Fused Quartz Data Sheet. http://www.momentiveperformancematerials.com/momentiveInternetDoc/Internet/Static%20Files/Chemical%20Composition.htm.
[85] F. Grønvold, E. F. Westrum Jr, *J. Chem. Thermodyn.* **1976**, *8*, 1039.

© 2012 WILEY-VCH Verlag GmbH & Co. KGaA, Weinheim
Adv. Energy Mater. **2012**,
DOI: 10.1002/aenm.201200043